Macromolecules **2008,** *41,* 1861−1871

Anomalous Sedimentation of Self-Avoiding Flexible Polymers

Xaver Schlagberger and Roland R. Netz*

Physics Department, Technical University Munich, 85748 Garching, Germany

Received April 23, 2007; Revised Manuscript Received December 31, 2007

ABSTRACT: We investigate the conformational changes of a single self-avoiding flexible polymer in strong sedimentation fields using hydrodynamic simulations and scaling arguments. For small fields or short chains hydrodynamic recirculation leads to compaction. For elevated fields or long chains the hydrodynamic drag leads to stretching of the coil and a decrease of the sedimentation coefficient for both linear and circular DNA, in agreement with results in ultracentrifuge experiments. At very large fields a spontaneous symmetry breaking takes place, and the polymer adopts a conformation consisting of a compact head and a trailing straight tail.

1. Introduction

For more than 80 years analytical ultracentrifugation has been used as a versatile tool for the characterization and separation of biomolecules.[1,2] In a sedimentation velocity experiment, one records the moving boundary of the investigated substance as a function of time to obtain the sedimentation coefficient S, which is defined as the radial velocity divided by the centrifugal force and is expected to reach a time-independent value for overdamped motion.[1] In the regime of very dilute solution we are interested in, interactions between macromolecules are negligible, such that mass and polymer conformation alone determine S. In a series of papers, it has been shown that dilute solutions of DNA with a molecular weight of more than 10^8 Da ($\approx 10^5$ base pairs) exhibit a decrease of S with increasing rotor speed, severely limiting the potential of the ultracentrifuge for analysis of long DNA.[3−6] This so-called sedimentation anomaly can be explained by inhomogeneous hydrodynamic drag forces within the chain:[7,8] The coil interior is hydrodynamically shielded while the chain ends, which on average are located at the coil exterior, receive more drag; consequently, the chain ends lag behind, the coil is stretched, and the sedimentation coefficient decreases. Shortly after the first experimental observation of the sedimentation anomaly, Zimm developed a theory for sedimenting chains based on the preaveraging approximation and utilizing the Gaussian phantom chain approximation. Zimm's theory[7] correctly predicts the functional dependence of S on rotor speed and molecular mass, but the initial quantitative agreement between theory and experiments[3,7] was later shown to be a coincidence.[6] More seriously, Zimm's preaveraging approximation (PAA) predicts a null effect for polymer rings, whereas experimentally the sedimentation coefficient of DNA loops exhibits an anomaly similar to linear chains.[9]

In this paper we study linear and circular sedimenting polymers using hydrodynamic simulations of a bead−spring model which is introduced in section 2. The resulting sedimentation behavior can be distinguished into several regimes: (i) For short self-avoiding chains compaction is caused by hydrodynamic chain recirculation. (ii) For longer chains and increasing fields the chain elongates slightly in the direction of motion, this constitutes the *weak-stretching regime*. (iii) In the *intermediate-stretching regime*, i.e. at even higher fields, the chain consists of a leading part that is more compact than the rest of the chain and a stretched trailing part. (iv) Finally, at very high fields, in the *strong-stretching regime*, the chain resembles a tadpole with a completely stretched tail.[10] In section 3 scaling laws of the chain radius and mobility (sedimentation coefficient) are presented for all regimes, which compare favorably with simulations and experiments for linear chains. The results are extended to circular chains in section 4. The formation of a compact and leading head constitutes a spontaneous symmetry breaking and leads to a reduction of the sedimentation coefficient both for linear and circular polymers, in agreement with experiments. In section 5, we implement Zimm's preaveraging model in the simulations and find the preaveraging to be a less serious approximation than the neglect of self-avoidance or chain inextensibility. In section 6, we briefly discuss the orientational order parameter, which can be measured in birefringence experiments, and in section 7, we touch upon effects due to a finite polymer bending rigidity. The results are compared with experiments in section 8.

2. Simulation Model

The (linear or circular) polymer is modeled as a chain of N spherical monomers subject to the Langevin equation (for the ith monomer)

$$\dot{\mathbf{r}}_i(t) = \sum_{j=1}^{N} \mu_{ij}\cdot[-\nabla_{\mathbf{r}_j} U(\{\mathbf{r}_N\}) + G\hat{e}_z] + \xi_i(t) \qquad (1)$$

where G is a constant force acting on each monomer, chosen to point along the z-direction. This force can be caused by electric fields acting on charged monomers or by gravitational force. Most relevant for experiments is the case where G is the sedimentation force per monomer, $G = m_0(1 - \rho_s/\rho_p)R_{UC}\,\omega^2$. In this equation, m_0 is the mass of one monomer, and ρ_s and ρ_p the densities of the solvent (water) and the polymer. R_{UC} is the radial distance from the center of the centrifuge and ω its angular velocity. The coupling to a heat bath is provided by vectorial Gaussian random velocities ξ_i with zero mean which are correlated according to the fluctuation−dissipation theorem as[12]

$$\langle \xi_i(t) \otimes \xi_j(t')\rangle = 2k_BT\delta(t - t')\mu_{ij} \qquad (2)$$

Hydrodynamic interactions between monomers i and j are included via the mobility tensor μ_{ij}: In most simulations we use for the off-diagonal components of the mobility matrix, $i \neq j$, the position-dependent Rotne−Prager tensor[13] for non-overlapping, $r_{ij} > 2a$

---

* To whom correspondence should be addressed.

10.1021/ma070947m CCC: \$40.75

$$\mu_{ij}^{(\mathrm{RP})} = \frac{1}{8\pi\eta r_{ij}}\left[\mathbf{I} + \frac{\mathbf{r}_{ij} \otimes \mathbf{r}_{ij}}{r_{ij}^{\ 2}} + \frac{2a^2}{r_{ij}^{\ 2}}\left(\frac{\mathbf{I}}{3} - \frac{\mathbf{r}_{ij} \otimes \mathbf{r}_{ij}}{r_{ij}^{\ 2}}\right)\right] \tag{3}$$

and overlapping spheres, $r_{ij} < 2a$

$$\mu_{ij}^{(\mathrm{RP})} = \frac{1}{6\pi\eta a}\left[\left(1 - \frac{9}{32}\frac{r_{ij}}{a}\right)\mathbf{I} + \frac{3r_{ij}}{32a}\frac{\mathbf{r}_{ij} \otimes \mathbf{r}_{ij}}{r_{ij}^{\ 2}}\right] \tag{4}$$

where $\mathbf{I}$ is the 3×3 unit matrix, η the solvent viscosity, and $r_{ij} = |\mathbf{r}_i - \mathbf{r}_j|$. As a test some simulations are done with Zimm's preaveraging approximation (PAA)[14] given by

$$\mu_{ij}^{(\mathrm{PAA})} = \frac{\mathbf{I}}{2\eta a\sqrt{6\pi^3|i-j|}}, \quad i \neq j \tag{5}$$

which is obtained from the Oseen tensor

$$\mu_{ij}^{(\mathrm{Os})} = \frac{1}{8\pi\eta r_{ij}}\left[\mathbf{I} + \frac{\mathbf{r}_{ij} \otimes \mathbf{r}_{ij}}{r_{ij}^{\ 2}}\right] \tag{6}$$

by averaging over the equilibrium conformation giving $\langle 1/r_{ij}\rangle = 1/(2a)\sqrt{6/(\pi|i-j|)}$. The self-part is in all cases given by the Stokes mobility of a sphere with radius a, $\mu_{ii} = \mathbf{I}/(6\pi\eta a) \equiv \mathbf{I}\mu_0$, where η denotes the solvent viscosity. The direct interaction potential

$$U = U_{\mathrm{LJ}} + U_{\mathrm{el}} \tag{7}$$

consists of a truncated Lennard-Jones potential to account for chain self-avoidance

$$U_{\mathrm{LJ}} = \epsilon_{\mathrm{LJ}}\sum_{i<j}\Theta(2a - r_{ij})\left[\frac{(2a)^{12}}{r_{ij}^{\ 12}} - \frac{2(2a)^6}{r_{ij}^{\ 6}} + 1\right] \tag{8}$$

and an elastic part U_{el} (springs between nearest neighbors), which for the freely jointed chain model (FJC) is given by

$$U_{\mathrm{el}}^{(\mathrm{FJC})} = \sum_{i=1}^{N-1}\frac{\gamma}{4a}[r_{ii+1} - 2a]^2 \tag{9}$$

and for the Gaussian chain model by

$$U_{\mathrm{el}}^{(\mathrm{Gauss})} = \sum_{i=1}^{N-1}\frac{\gamma}{4a}r_{ii+1}^{\ \ 2} \tag{10}$$

In the above, $\Theta(x)$ is the Heavyside step function. A stretching modulus of $\gamma = 400k_{\mathrm{B}}T/a$ for $G \leq k_{\mathrm{B}}T/a$ and $\gamma = 400G$ for $G > k_{\mathrm{B}}T/a$ is sufficient to approximate the FJC model with essentially constant bond length. For the Gaussian chain model we set $\gamma = 3k_{\mathrm{B}}T/(2a)$, giving an equilibrium mean-squared bond length of $\sqrt{\langle r_{ii+1}^{\ \ 2}\rangle} = 2a$. For a self-avoiding (SA) chain, the repulsive potential strength is chosen as $\epsilon_{\mathrm{LJ}} = k_{\mathrm{B}}T$; the phantom chain (PC) is realized for $\epsilon_{\mathrm{LJ}} = 0$.

In the simulations we discretize eq 1 with a time step Δ and make all variables unitless by rescaling with monomer size a and thermal energy $k_{\mathrm{B}}T$ according to $\tilde{\gamma} = \gamma a/k_{\mathrm{B}}T$ and $\tilde{G} = Ga/k_{\mathrm{B}}T$. The only parameter involving the solvent viscosity is the rescaled time step $\tilde{\Delta} = \Delta\mu_0 k_{\mathrm{B}}T/a^2$. The continuum limit of the Langevin equation eq 1 is reached for $\tilde{\Delta} \rightarrow 0$ in which limit all results become independent of solvent viscosity. Depending on chain length and field strength, we choose $\tilde{\Delta}$ between 3×10^{-5} and 0.005. For the FJC mode we adapt $\tilde{\gamma}$ to $\tilde{G}$ at large sedimentation fields since this allows using maximally large time steps and thus increases the simulation efficiency.

We use the Brownian dynamics algorithm by Ermak and McCammon[12] where the correlated random numbers of eq 2 are generated by multiplying independent Gaussian random numbers with the triangle matrix resulting from a Cholesky decomposition of the matrix μ_{ij}. Being the most time-consuming part in the simulation, the decomposition is done only every tenth time step. It was checked that this approximation has only a minor effect, in particular, that the fluctuation−dissipation theorem in the form of eq 2 is still valid within error bars. The chains are first equilibrated with a slowly increasing field before averages are taken. The total simulation consists of up to 10^8 steps. Errors are calculated using block averaging and only shown if larger than the symbol size. For the longest chains, $N = 200$ and $N = 400$, the simulation of one parameter set took up to 2 weeks on a 64-bit workstation.

In sedimentation experiments, the sedimentation coefficient is defined as

$$S^{\mathrm{exp}} = \frac{v}{R_{\mathrm{UC}}\omega^2} \tag{11}$$

where v is the velocity of the molecule; R_{UC} and ω are again the radial distance and angular velocity of the centrifuge. Because masses do not appear within the position-Langevin equation framework, we consider the following modified sedimentation coefficient $S = v/G = S^{\mathrm{exp}}/[m_0(1 - \rho_{\mathrm{s}}/\rho_{\mathrm{p}})]$ which in rescaled form reads

$$\tilde{S} \equiv S/\mu_0 = \sum_i\langle\dot{\mathbf{r}}_i\rangle/(N\tilde{G}) \tag{12}$$

where the sum runs over all monomers i of the molecule.

3. Results for Linear Chains

In this section we concentrate on a *linear* SA-FJC with full hydrodynamic interactions (HI) as obtained with the mobility tensor on the Rotne−Prager level in eqs 3 and 4. In a later section we will extend the results to circular chains.

Figure 1a shows the rescaled sedimentation coefficient $\tilde{S}$ as a function of the rescaled sedimentation field $\tilde{G}$ on a semilogarithmic scale for chains with $N = 10$ to $N = 200$ monomers. With the exception of $N = 10$ and $N = 20$, $\tilde{S}$ displays a nonmonotonic behavior: For small fields, $\tilde{S}$ increases slightly due to a beginning compaction of the chain. This can be seen in Figure 1b from the initial decrease of the radius of gyration, R_{g}

$$R_{\mathrm{g}}^{\ 2} = \frac{1}{N}\sum_i(\mathbf{r}_i - \mathbf{R}_{\mathrm{M}})^2 \tag{13}$$

where $\mathbf{R}_{\mathrm{M}} = \sum_i\mathbf{r}_i/N$ is the center of mass. Note that in equilibrium, i.e., for $\tilde{G} = 0$, one expects a scaling $R_{\mathrm{g}} \sim N^{\nu}$ with $\nu = 3/5$.[14] Accordingly, the results for R_{g} have been rescaled by N^{ν}, yielding good scaling for small fields $\tilde{G}$. As seen in Figure 1a, after passing through a maximum, $\tilde{S}$ drops considerably and saturates at a much lower value than for the unperturbed ($\tilde{G} \rightarrow 0$) chain. This is paralleled by a sharp increase in R_{g}, which defines a critical field $\tilde{G}^{\star}$ at which a chain starts to unfold. The curve $\tilde{S}$ for the longest chain ($N = 200$) forms an upper envelope for the shorter chains, which means that at a given rotor speed longer chains are always faster than shorter ones. Thus, contrary to earlier expectations,[4,5,11] S displays no maximum as a function of length for a given rotor speed.

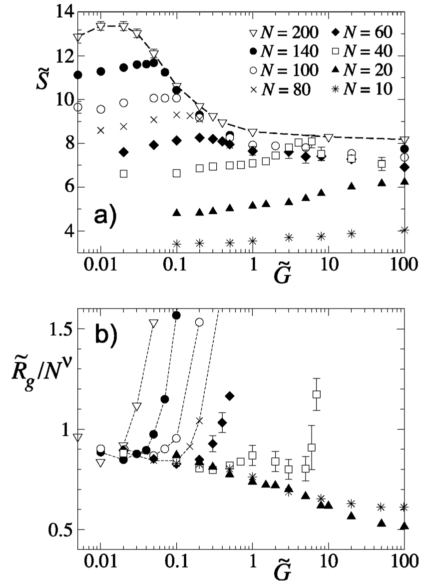

Figure 1. (a) Sedimentation coefficient $\tilde{S}$ of a linear self-avoiding FJC for several monomer numbers N as a function of sedimenting field $\tilde{G} = Ga/k_BT$. The $N = 200$ results (broken line) give an upper envelope. (b) Reduced radius of gyration R_g/aN^ν (using $\nu = 3/5$) for the same parameters as in (a), showing an initial chain compaction and (for larger G) a chain stretching.

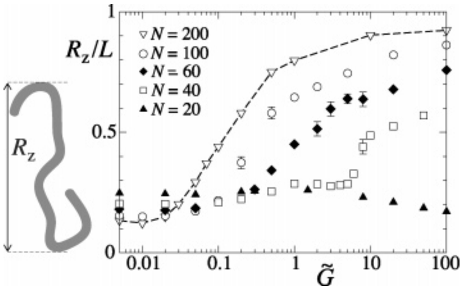

Figure 2. Relative root-mean-square maximum extension in field direction, R_z/L (see sketch), as a measure for the unfolding of the linear chains. The $N = 200$ points are connected for better visibility.

While the radius of gyration is a useful quantity to show the compaction and initial stage of stretching of the coil, the unfolding is better described by the relative extension R_z/L, where $L = 2aN$ is the contour length and R_z is defined as the root-mean-square of the maximum extension in z-direction:

$$R_z^2 = \langle \max_{\{ij\}}^2 [r_{i,z} - r_{j,z}] \rangle \tag{14}$$

Figure 2 shows that the unfolding is not abrupt; instead, there is an intermediate range where the polymer is stretched but not fully extended. In the case of $N = 100$ it starts at about $\tilde{G} \approx 0.1$ and ends at about $\tilde{G} \approx 10$. It is interesting to note that the limiting relative chain extension $\lim_{\tilde{G}\to\infty}(R_z/L)$ approaches unity only for $N \to \infty$; finite-N chains do not unfold completely even at very high forces. This is related to the fact that chains form a tadpole structure with a relatively compact head region, even at high sedimentation fields, as will be further discussed below.

Snapshots in Figure 3a visualize the progressive chain stretching with growing $\tilde{G}$ for $N = 100$: At $\tilde{G} = 0.01$ the chain is only slightly perturbed from its equilibrium random coil structure; at $\tilde{G} = 0.1$ and $\tilde{G} = 1$ the chain is partially unfolded, and a head and tail region can already be discerned; in the limit of strong forces, e.g., $\tilde{G} = 100$, a tadpole structure is stabilized by hydrodynamic effects. The stretching starts earlier for longer chains as seen in Figure 3b. A slight compaction is realized at even smaller fields; yet for long chains, complete compaction is preempted by chain stretching. We are now going to investigate these regimes in more detail. It is important to note that both self-avoidance and hydrodynamic interactions are crucial to observe the spontaneous symmetry-breaking into a compact head and a stretched tail. We will discuss phantom chains and the preaveraging approximation in detail in section 5.

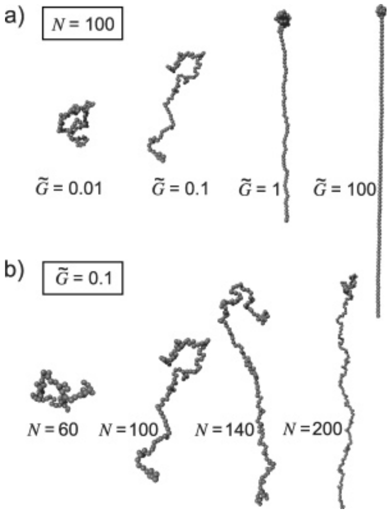

Figure 3. (a) Typical chain configurations for monomer number $N = 100$ at different field strengths (polymers move upward, drawn to scale). (b) Simulation snapshots at sedimentation field strength $\tilde{G} = 0.1$ for different N (drawn not to scale).

3.1. Unfolding in Strong Centrifugal Fields. In the limit of very large driving field $\tilde{G}$ the chain adopts a "tadpole" configuration consisting of a compact head of N_h monomers followed by a straight tail of $N_t = N - N_h$ monomers as in the $\tilde{G} = 1$ case of Figure 3a. Similar conformations are observed in a different context when a collapsed chain that is fixed at one end is stretched by an external force.[15] In that case the symmetry breaking between compact head and stretched tail is imposed by the external boundary condition; in our case it is spontaneously brought about by hydrodynamic interactions, as will be discussed further below. From the tail stretching it follows that the head pulls the tail with a force F_s, which also orients the tadpole given $F_sR_z > k_BT$. Neglecting hydrodynamic interactions between head and tail, which only contribute to higher-order corrections, the head velocity is obtained as the product of the total direct force on the head, $GN_h - F_s$, times the head mobility $\mu_{sph} = \mu_0 a/R_h$, which is just the mobility of a sphere with radius R_h

$$v_h \simeq (GN_h - F_s)\frac{\mu_0 a}{R_h} \simeq (GN_h - F_s)N_h^{-\nu}\mu_0 \tag{15}$$

where $R_h \sim aN_h^\nu$ is the radius of the head and ν in the range $1/3 < \nu < 3/5$, depending on whether the head is a globule or a self-avoiding coil. Using the mobility of a long straight cylinder with long axis aN_t and short axis a moving in the direction of its long axis[16]

$$\mu_{cyl} \approx \frac{3\mu_0}{2N_t}(\ln N_t - 0.207) \tag{16}$$

and a total direct force of $GN_t + F_s$, the tail velocity is

$$v_t \simeq (GN_t + F_s)\frac{3\mu_0}{2N_t}[\ln N_t - 0.207] \tag{17}$$

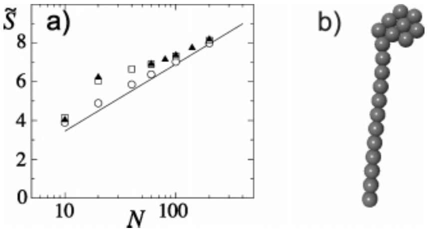

Figure 4. (a) Zero temperature (averaged over initial conditions, squares) and finite-temperature simulations ($\tilde{G} = 100$, filled triangles) compared with the asymptotic scaling law eq 19, $\tilde{S} \sim (3/2) \ln N$ (solid line). Circles represent zero-temperature simulations where the initial configuration is a straight chain at an angle of 45° to the *z*-axis, leading to two-dimensional stable stationary configurations like the one in (b) for $N = 20$.

Equations 15−17 describe the stationary state. To understand the stretching force F_s, it is helpful to look at the kinetic pathway of tadpole formation: A long chain in a strong sedimentation field that is initially in a random coil configuration becomes more compact, recirculates, and finally unfolds to form a tadpole structure.[17] The recirculation mechanism is described in more detail in section 3.4. Since attractive monomer−monomer interactions are absent, the stretching force F_s is solely produced by internal friction in the head. It maximally scales as $F_s \sim GN_h$ because at this magnitude the head would come to a complete stop (eliminating the recirculation and thus the cause for the frictional force in the first place). To leading order in our scaling argumentation, we can thus neglect F_s in the above velocity expressions. In the stationary state head and tail velocities are equal, $\upsilon_h = \upsilon_t \equiv \upsilon$, which leads to a logarithmically small head size using eqs 15 and 17:

$$N_h \simeq \left(\frac{3}{2} \ln N\right)^{1/(1-\nu)} \tag{18}$$

From the definition eq 11 and the expression eq 15 we find a sedimentation coefficient of

$$\tilde{S} \simeq \frac{\upsilon}{G\mu_0} \simeq \frac{3}{2} \ln N \tag{19}$$

In order to directly test the large-field result eq 19, we perform zero-temperature simulations for the SA-FJC where the noise term ξ_i in eq 1 is omitted, choosing rescaled parameters $\gamma = 200\ G$ and $\epsilon_{LJ} = Ga$. At zero temperature, a complete sampling of the phase space is not achieved, and the results depend on the initial conditions: If, e.g., the chains are initially straight and at a finite angle (45°) with respect to the sedimentation field, all chains (even $N = 10$) roll up to form a two-dimensional tadpole conformation, similar to the representative snapshot shown in Figure 4b. The resulting sedimentation coefficients are shown in Figure 4a (circles) and compare very well with the asymptotic result eq 19 (solid line). If we average over random initial configurations, the zero-temperature dynamics (squares) resembles in most cases the finite-temperature dynamics for very high fields, $\tilde{G} = 100$, which are taken from Figure 1a (triangles), but the asymptotic scaling law eq 19 is approached much slower and only for $N \gg 1$.

In trying to understand why the tadpole structure forms, one is led back to the question of the stability of different conformations with respect to small perturbations. As is easy to see, the tadpole configuration is hydrodynamically stable with respect to small perturbations of the head/tail size ratio and the orientation: In the case of a tadpole oriented with the head in front and a trailing tail, a head slightly larger than in the stationary state, as determined by $\upsilon_h \sim \upsilon_t$, will move faster than the tail, thus unwinding the head and bringing its size back to its equilibrium value (and conversely: a head in front and slightly smaller than the equilibrium value will slow down and thus push into the tail and grow in size). If, on the other hand, the tail is in front, a slightly smaller head will slow down and completely unwind, while a larger head will gain relative speed and overtake and eventually swallow the tail. This shows that the tadpole with the head in front is a hydrodynamically stabilized structure. Incidentally, similar structures are observed with sedimenting fluid droplets.

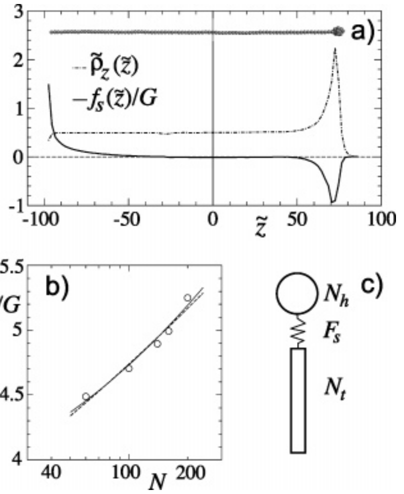

Figure 5. Stretching force within chain. (a) Average elastic force per monomer $f_s(\tilde{z})$ according to eq 20 (solid line) and the one-dimensional projected monomer density $\tilde{\rho}_z(\tilde{z})$ (dotted-dashed line) as a function of distance $\tilde{z}$ from the center of mass for a $N = 100$ SA-FJC at field $\tilde{G} = 100$. Integrating f_s from the tail to $\tilde{z} = 0$ gives the stretching force F_s, defined in eq 21, which is a measure for the elastic force between head and tail. A snapshot illustrates the relative position along the chain. (b) F_s displays a logarithmic dependence on N at $\tilde{G} = 100$ as shown by two fits: $F_s/G = 3.64 + 0.024(\ln N)^{2.5}$ (solid line) and $F_s/G = 1.9 + 0.186\ (\ln N)^{1.5}$ (dashed line). (c) Sketch of the tadpole model. A stretching force F_s acts between the head and the tail.

It remains to justify the scaling assumption for the stretching force acting on the tail, $F_s \sim GN_h$, which we use in fact, also for small and intermediate fields. This is complicated for two reasons: (i) The boundary between head and tail is not clearly defined, especially for intermediate fields. We thus restrict ourselves to the case $\tilde{G} = 100$ where the chain is nearly completely unfolded. (ii) The force distribution along the chain is complex and nonmonotonic as can be seen in Figure 5a. Here $f_s(\tilde{z})$ is the average elastic force per monomer at $\tilde{z}$

$$f_s(\tilde{z}) = \left\langle -\frac{\partial}{\partial z_i} U_{el}^{(FJC)} \middle| \tilde{z}_i = \tilde{z} \right\rangle \tag{20}$$

where the average is taken over all monomers i and conformations. In our notation, $\tilde{z}$ is the (rescaled) distance from the center of mass in field direction. Monomers in the region close to the head are pulled backward, i.e., toward the tail, by elastic forces f_s as can be seen by the fact that f_s is negative. Note that the average velocity of all monomers is the same, so the negative stretching forces are made up for by increased hydrodynamic drag due to the close vicinity of the head. The opposite is true for monomers located at the end of the tail; here the elastic force f_s is positive, and the monomers are pulled in the direction of the head. The one-dimensional rescaled monomer density $\tilde{\rho}_z(\tilde{z})$, defined as the average number of monomers per rescaled unit length, has a value $\tilde{\rho}_z(\tilde{z}) \approx 1/2$ in the tail region, corresponding to one monomer per average bond length, and a smeared-out peak at the location of the head. The smearing of the head density maximum is due to thermal fluctuations of the tail length, which are small but still present at $\tilde{G} = 100$. For the stretching force between head and tail F_s (see Figure 5c) we use the following definition:

$$F_s = \int_{-\infty}^{0} \tilde{\rho}_z(\tilde{z})\, f_s(\tilde{z})\, d\tilde{z} \tag{21}$$

which is the total elastic force between all segments below the center of mass ($\tilde{z} = 0$) and above the center of mass. In Figure 5b this overall stretching force is shown as a function of N at $\tilde{G} = 100$ and fitted to $F_s/G = a_0 + a_1(\ln N)^{1/(1-\nu)}$ with fit parameters $a_0 = 3.64$ and $a_1 = 0.024$ for $\nu = 3/5$, solid line, and $a_0 = 1.9$ and $a_1 = 0.186$ for $\nu = 1/3$, broken line. For $N \gg 1$ the data for F_s show a logarithmic dependence on N and are thus consistent with $F_s/G \sim (\ln N)^{1/(1-\nu)} \sim N_h$ for both values of ν for this restricted data set. Note that the result eq 19 is independent of the precise value of ν.

3.2. Ellipsoids in Small Centrifugal Fields. The rescaled fields $\tilde{G}$ accessible in experiments on normal polymers are much below unity (as explained in the Discussion section). Anomalous sedimentation can therefore only be observed for very long chains, in which case the deformation of the coil and the decrease of S are still small. In the snapshot Figure 3a for $N = 100$ and $\tilde{G} = 0.1$ one can see that the boundary between head and tail is diffuse and that the tail is slightly perturbed into an ellipsoid with short axis R_t and long axis L_t (see definition in Figure 6c). We assume that the perturbation is weak enough such that $R_t \sim aN_t^{\nu}$ still holds. As before, we assume that all monomers in the head contribute via internal friction to the stretching force F_s, i.e. $F_s \sim N_h G$. We again calculate separately head velocity v_h and tail velocity v_t. From eq 15 and neglecting the correction due to the finite stretching force, we obtain for the head velocity

$$v_h \sim G N_h^{1-\nu} \mu_0 \tag{22}$$

The tail velocity follows from the mobility of an ellipsoid along its long axis in the weak-asymmetry limit $\epsilon \equiv (L_t/R_t) - 1 \lll 1$,[18] $\mu_{ell} = [6\pi\eta R_t(1 + \epsilon/5)]^{-1}$, leading to

$$v_t \sim G N_t \mu_0 \frac{a}{R_t(1 + L_t/4R_t)} \tag{23}$$

For small stretching forces, $F_s \ll k_B T/R_t$, the tail stretching is harmonic: The mean square extension of the ellipsoid in force direction $\langle L_t^2 \rangle$ differs from its zero-force value $\langle L_t^2 \rangle_0$ by a term quadratic in F_s, $\langle L_t^2 \rangle \sim \langle L_t^2 \rangle_0 [1 + \langle L_t^2 \rangle_0 (F_s/k_B T)^2]$.[19] Using the same name for the random variable L_t and its root-mean-square, $\langle L_t^2 \rangle \equiv L_t^2$, and assuming that the lateral extension of the ellipsoid is unperturbed by the stretching force, $R_t^2 = \langle L_t^2 \rangle_0$, we find at the lowest order in F_s

$$L_t/R_t - 1 \sim (F_s R_t/kT)^2 \tag{24}$$

This defines the weak-stretching regime, valid for $F_s < k_B T/L_t$ and thus for $\tilde{G} \ll N^{-1-\nu}$. Requiring head and tail to move at the same speed, $v_h = v_t$, and using eqs 22−24, we obtain to lowest order in $F_s R_t/k_B T$

$$N_h \sim \frac{N}{2}[1 - cN^{2+2\nu}\tilde{G}^2] \tag{25}$$

where c is a numerical constant which is determined from a fit to the numerical data. Inserting eq 25 into eq 22 gives

$$\tilde{S} \simeq c_1 N^{1-\nu} - c_2 N^{3+\nu} \tilde{G}^2 \tag{26}$$

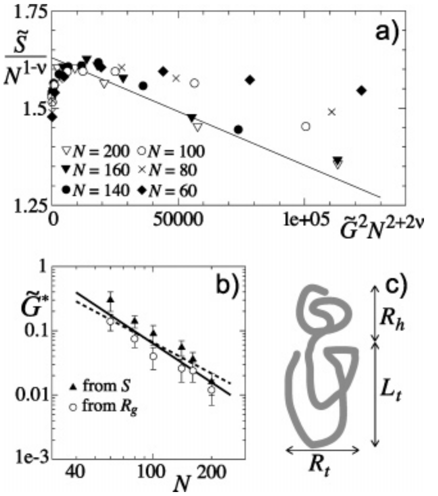

Figure 6. Small fields: (a) Scaling plot of the low-field data from Figure 1a; the solid line is given by $\tilde{S}/N^{1-\nu} = 1.63 - 2.77 \times 10^{-6} \tilde{G}^2 N^{2+2\nu}$ and obtained by an asymptotic fit to the $N = 200$ data. (b) Unfolding field strength $\tilde{G}^\star$, defined graphically in Figure 1 from the maximum of S (triangles) and the minimum of R_g (circles). The solid line is a heuristic fit to both data sets with $\tilde{G}^\star = 670N^{-2}$ and the broken line denotes $\tilde{G}^\star = 100\, N^{-1-\nu}$. (c) Definition of head size R_h, tail length L_t, and tail width R_t.

with $\nu = 3/5$ and coefficients c_1 and c_2 to be determined later. The N dependence of the correction factor, $N^{3+\nu}$, is in accord with experiments, where a scaling proportional to $N^{3.65}G^2$ is observed,[3] and for the longest chains also in satisfactory agreement with an asymptotic fit to the simulation data in Figure 6a, where coefficients $c_1 = 1.63$ and $c_2 = 2.77 \times 10^{-6}$ are obtained. Note that in our previous publication the less accurate value of $c_1 = 1.68$ was obtained for $\lim_{\tilde{G}\to 0} \tilde{S}/N^{1-\nu}$.[20] For slightly overlapping (10%) beads Monte Carlo simulations[21] give an equilibrium value fit of $\tilde{S} = c_1 N^{1-\nu}$ with $c_1 = 1.805 \pm 0.033$ and $\nu = 0.586 \pm 0.005$, which illustrates that c_1 is not universal, in contrast to the product of rescaled sedimentation coefficient and radius of gyration $\tilde{S}R_g$, where the dependence on the specific model largely cancels out (see e.g. ref 22).

3.3. Partial Stretching in Intermediate Fields. For intermediate stretching forces, $k_B T/L_t < F_s < k_B T/a$, the tail is stretched but not fully extended. Using the assumption $F_s \sim GN_h$ and the scaling $L_t \sim R_t \sim aN_t^{\nu}$ and $N_h \sim N_t \sim N/2$ in the weak-stretching regime as well as eq 18 in the strong-stretching regime, this range corresponds to $\tilde{G}^{\star\star} < \tilde{G} < \tilde{G}^{\star\star\star}$ with

$$\tilde{G}^{\star\star} \sim N^{-1-\nu} \tag{27}$$

and

$$\tilde{G}^{\star\star\star} \sim (\ln N)^{1/(\nu-1)} \tag{28}$$

$\tilde{G}^{\star\star}$ is thus the field strength at which the weak-stretching regime eq 26 ends and $\tilde{G}^{\star\star\star}$ the field at which the tail becomes completely stretched with $L_t \sim aN_t$. The actual onset of chain unfolding $\tilde{G}^\star$, which is determined from the maximum in S or the minimum in R_g (cf. Figure 1), is shown in Figure 6b and follows in the restricted available data range the expression

$$\tilde{G}^\star = 670N^{-2} \tag{29}$$

as shown by the solid line. Note that this scaling form implies that $\tilde{G}^\star < \tilde{G}^{\star\star}$ for large N. Still within the error bars is the scaling

$$\tilde{G}^\star = 100N^{-1-\nu} \tag{30}$$

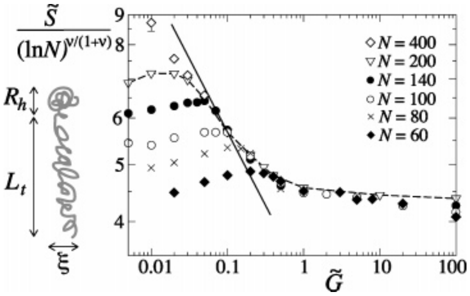

Figure 7. Intermediate field: rescaled data of Figure 1a plus four additional data points for monomer number $N = 400$ (rescaling done using $\nu = 3/5$). An intermediate scaling regime as described by eq 34 (solid line) is approached for long chains. The left drawing defines the head size, tail length, blob size, R_h, L_t, and ξ, in the intermediate stretching regime.

as shown by the broken line, which would correspond to $\tilde{G}^\star \sim \tilde{G}^{\star\star}$. Within the limited range of data available, no clear decision between the two scaling forms is possible.

In the intermediate-field regime the length of the tail scales as[23]

$$L_t \sim aN_t(F_s a/k_B T)^{(1-\nu)/\nu} \tag{31}$$

We assume that the tail is already stretched enough to be described by a cylinder

$$v_t \sim GN_t \frac{\mu_0 a}{L_t}[\ln(L_t/\xi) - 0.207] \tag{32}$$

where $\xi \sim ak_BT/(F_s a)$ is the blob size in the tail, i.e., the diameter of the cylinder (see sketch in Figure 7). Here we neglect the roughness of the tail. In the intermediate stretching regime ξ is independent of the chain length, which yields a factor $L_t/\xi \sim N_t$ inside the logarithm. Together with $v_h \sim GN_h^{1-\nu}\mu_0$ as in eqs 15 and 22, we find for $N_t \gg N_h$ and thus $N_t \approx N$ a head size of

$$N_h \sim \tilde{G}^{-1/(1+\nu)}(\ln N)^{\nu/(1-\nu^2)} \tag{33}$$

which yields a sedimentation coefficient of

$$\tilde{S} \sim \tilde{G}^{(\nu-1)/(\nu+1)}(\ln N)^{\nu/(\nu+1)} \tag{34}$$

This complements the results in eqs 19 and 26 in the strong and weak stretching limits, respectively. The scaling is consistent with simulations if extrapolated to very long chains as seen in Figure 7: For $N \leq 200$ the exponent $(\nu - 1)/(\nu + 1)$ of $\tilde{G}$ is not reached because of slow crossovers, but the four data points for $N = 400$ suggest that longer chains might indeed be described by eq 34, which is indicated by a straight line. At $\tilde{G} \approx 0.1$ the sedimentation coefficients shows a weak dependence on N: Longer chains are faster than short ones (see Figure 7).

As has been noted in the literature before, eq 26 predicts a nonmonotonic dependence of the sedimentation velocity on the chain length N. In fact, the crossover between increasing and decreasing dependence on N is determined by $\partial\tilde{S}/\partial N = 0$, which leads to a threshold field of $\tilde{G} \approx 256\ N^{-1-\nu}$ (using the numerically determined constants c_1 and c_2 of Figure 6) and has thus the same scaling as $\tilde{G}^{\star\star}$ but is larger than $\tilde{G}^\star$ of eq 30. However, this conclusion is faulty in an essential aspect: the small-field (or weak-stretching) regime ends before $\tilde{G} = 256\ N^{-1-\nu}$, viz. $\tilde{G}^2N^{2+\nu} \approx 6.5 \times 10^4$, is reached. This is appreciated most clearly in Figure 6a, where it is seen that the $N = 200$ data points are described by the line eq 26 only up to $\tilde{G}^2N^{2+\nu} \approx 6 \times 10^4$; for higher fields strong deviations are seen. The small-field result in eq 26 thus becomes invalid before the plateau defined by $\partial\tilde{S}/\partial N = 0$ is reached. So the tentative conclusion is that longer chains always sediment faster than short chains, in line with our simulation results.

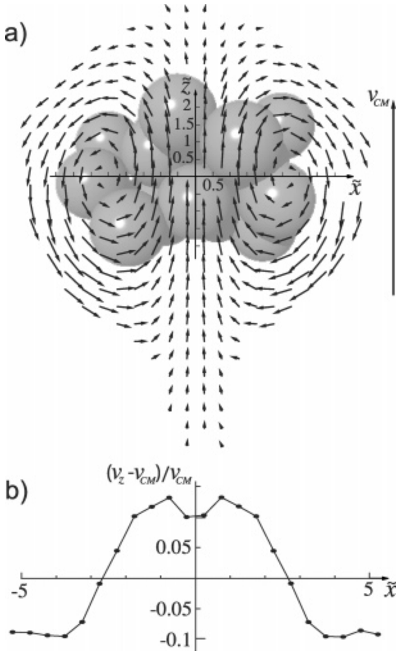

Figure 8. (a) Simulated velocity field in the $x-z$ plane (for a cut at position $y = 0$) of a $N = 20$ globule at zero temperature, averaged over 100 runs with random initial conditions. The coordinate origin is chosen as the center of mass. The arrow directions indicate the local direction of the polymer velocity, measured with respect to the center-of-mass velocity. The lengths of the vectors are proportional to the local average velocity (not to be confused with the monomer flux). Arrows are only drawn at location where the probability to find a monomer is larger than 0.002. In the background, a typical snapshot is shown. (b) Relative monomer velocity in field direction, $v_z - v_{CM}$, measured in units of the v_{CM} as a function of $\tilde{x}$ along the line with coordinates $y = z = 0$ for the same system as in (a).

Tadpole orientation and conformational stability require the torque $M \sim F_sL_t$ to be larger than k_BT. For $F_s \sim GN_h$, $L_t \sim N_t^\nu$, and $N_t \sim N_h \sim N$—valid within the weak-stretching regime—this is equivalent to $\tilde{G} > N^{-1-\nu}$ and coincides with the crossover between weak and intermediate stretching. In other words, the tadpole structure in the intermediate stretching regime is stable and shows only little conformational and orientational fluctuations. In the weak-stretching regime orientational fluctuations are frequent but the scaling of the orientationally averaged chain stretching is unchanged.

3.4. Compaction. Prior to stretching, i.e., for $G < G^\star$, a slight compaction of long sedimenting chains occurs (see data for the radius of gyration for $N = 60$ in Figure 1b) for which we now present a blob argument. In the nondraining regime, a chain of radius R sediments with a velocity given by Stokes' law[14]

$$v \sim \mu_0 GNa/R \tag{35}$$

The hydrodynamic drag acts primarily on peripheral chain segments, inducing internal chain recirculation with a typical velocity scale v. Figure 8a shows the velocity field of the monomers of a $N = 20$ polymer globule at zero temperature in the center-of-mass frame. The diagram is obtained in the following way: The space is partitioned into cubes of size $0.5a \times 0.5a \times 0.5a$ within which the average monomer velocity is calculated. At each time step, we calculate the center-of-mass velocity v_{CM} and from that the relative velocities with respect to v_{CM} of all monomers in the respective cubes and average over time and initial conditions. Cubes that are populated with less than 0.002 monomers on average are omitted in the plot. A polymer circulation in the $y = 0$ plane is clearly visible in the figure. Noteworthy is the partial unfolding and backfolding of the chain and the weak formation of a tail in the lower part of the plot. In the background, we show a typical chain snapshot. The recirculation can also be seen in the velocity component v_z (determined again with respect to the center-of-mass velocity v_{CM}) as a function of the lateral coordinate $\tilde{x}$ through the chain center of mass (i.e., for $y = z = 0$), which is plotted in (b). Monomers close to the center, i.e., small $|\tilde{x}|$, move faster, outer monomers slower than the center-of-mass velocity v_{CM}.

We partition the chain into blobs consisting of g monomers and unperturbed size

$$\xi \sim a g^{\nu} \tag{36}$$

The assumption of equilibrium scaling inside blobs holds as long as the recirculation time

$$\tau_{\mathrm{V}} \sim \xi / v \tag{37}$$

is larger than the blob relaxation time τ_{R}, the blob size thus follows from $\tau_{\mathrm{R}} \sim \tau_{\mathrm{V}}$. Neglecting entanglement effects and enhanced friction inside the polymer coil, the blob relaxation time is

$$\tau_{\mathrm{R}} \sim \xi^3/(a \mu_0 k_{\mathrm{B}} T) \tag{38}$$

which corresponds to the time it takes for a blob to diffuse over its own size. Equating the relaxation and recirculation times leads to

$$\xi^2 \sim k_{\mathrm{B}} T R/(G N) \tag{39}$$

Beyond the blob size, the chain cannot relax and is condensed by the recirculation shear, suggesting compact scaling

$$R \sim \xi (N/g)^{1/3} \tag{40}$$

At $\tilde{G} \simeq \tilde{G}_{<}^{\mathrm{com}}$ the blob size reaches R, which from eq 39 using $R \sim a N^{\nu}$ gives

$$\tilde{G}_{<}^{\mathrm{com}} \sim N^{-1-\nu} \tag{41}$$

For smaller fields, $\tilde{G} < \tilde{G}_{<}^{\mathrm{com}}$, the blob size is larger than the chain radius, $g > N$, and the chain conformation is unperturbed by sedimentation; for larger fields, $\tilde{G} > \tilde{G}_{<}^{\mathrm{com}}$, compaction is predicted. Combining eqs 36, 39, and 40, the chain radius and blob size scale as

$$R \sim a N^{(1-\nu)/(3\nu+1)} \tilde{G}^{(1-3\nu)/(3\nu+1)}, \quad \tilde{G} > \tilde{G}_{<}^{\mathrm{com}} \tag{42}$$

$$\xi \sim a N^{-2\nu/(3\nu+1)} \tilde{G}^{-3\nu/(3\nu+1)}, \quad \tilde{G} > \tilde{G}_{<}^{\mathrm{com}} \tag{43}$$

For $\nu = 3/5$ these equations reduce to $R \sim a N^{1/7} \tilde{G}^{-2/7}$ and $\xi \sim a N^{-3/7} \tilde{G}^{-9/14}$. Equations 42 and 43 are only valid until $\xi \sim a$. For longer chains or higher fields the chain scales like a compact object, $R \sim a N^{1/3}$, and the sedimentation constant and radius of gyration approach a constant value (data points for $N = 10$ and $N = 20$ in Figure 1). This happens for $\tilde{G} > \tilde{G}_{>}^{\mathrm{com}} \sim N^{-2/3}$.

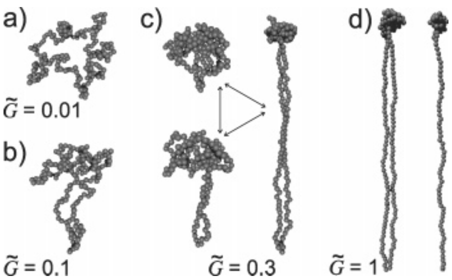

Figure 9. Snapshots for a $N = 200$ circular self-avoiding freely jointed chain (SA-FJC) with full hydrodynamic interactions (HI) at different sedimentation field strengths $\tilde{G}$. In c) for $\tilde{G} = 0.3$ the chain conformation oscillates between a globular and an unfolded state. In (d) for $\tilde{G} = 1$ also a linear chain with $N = 100$ is shown for comparison.

The scaling $\tilde{G}^{\star} \sim N^{-2}$ seen in Figure 6b is at odds with the expectation $\tilde{G}_{<}^{\mathrm{com}} < \tilde{G}^{\star}$ with $\tilde{G}_{<}^{\mathrm{com}}$ given in eq 41. This is based on the observation of compactified chains for an intermediate range of sedimentation fields G in the simulations which would suggest that the threshold for compaction $\tilde{G}_{<}^{\mathrm{com}}$ is smaller than the unfolding transition $\tilde{G}^{\star}$. This could mean that (i) the apparent scaling of $\tilde{G}^{\star}$ in Figure 6b is due to some crossover only observed for short chains and that even the slight compaction is preempted by chain unfolding in the limit of long chains, except locally in the head region. In this scenario no compaction would be observed for long chains, and the chain would be stretched even for infinitesimally weak fields. DNA sedimentation experiments support this explanation since a rotor speed dependent increase of the sedimentation coefficient has not been observed so far. (ii) Alternatively, the threshold for compaction $\tilde{G}_{<}^{\mathrm{com}}$ could be lower than suggested by our scaling result $\tilde{G}_{<}^{\mathrm{com}} \sim N^{-1-\nu}$, which is plausible since it neglects entanglement effects, or $\tilde{G}^{\star}$ could scale differently than given in eq 29. In this scenario, a range $\tilde{G}_{<}^{\mathrm{com}} < \tilde{G} < \tilde{G}^{\star}$ of beginning compaction exists. It is unlikely that simulations will help to resolve this issue; we need experimental results for well characterized model systems.

4. Circular Polymers

Up to now we treated only linear chains; it will be shown in this section that many of the results obtained so far for linear chains also apply to *circular* SA-FJC. It is known experimentally that circular DNA exhibits a rotor speed dependence of the sedimentation constant similar to linear DNA with half the length.[9] Circular chains are also relevant in the context of DNA supercoiling and bacterial nucleoids.[24,25] The series of conformations for circular $N = 200$ chains at different field strengths in Figure 9 is similar to the series of linear $N = 100$ chains in Figure 3a. A direct comparison is made in Figure 9d at a driving force $\tilde{G} = 1$: The circular chain with $N = 200$ forms a tadpole similar in size and shape to the linear $N = 100$ chain except that the tail is double-stranded. Noteworthy are the conformations at $\tilde{G} = 0.3$: The chain is already rather compact but temporarily unfolds and folds back. At stronger $\tilde{G}$ the unfolded state is more stable; the compact states are less often explored. Such a behavior is also observed for linear $N = 100$ chains, but in that case less pronounced.

In Figure 10, we compare (a) $\tilde{S}$ and (c) R_z/L for circular chains of different lengths (open symbols) with the result for a linear chain with $N = 100$ (filled circles). Most importantly, chain compaction is more pronounced for circular chains, as witnessed by the increase of sedimentation coefficient $\tilde{S}$ for intermediate $\tilde{G}$. The reason for this is unclear, but must have to do with the chain topology which might favor chain entanglements. The circular $N = 200$ chain (open triangles) starts unfolding at a slightly higher force than the linear $N = 100$ chain (filled circles), since entanglement effects are stronger for the former. At strong $\tilde{G}$, $\tilde{S}$ is ∼2 times larger for the $N = 200$ chain because the sedimentation coefficient of an unfolded chain is besides

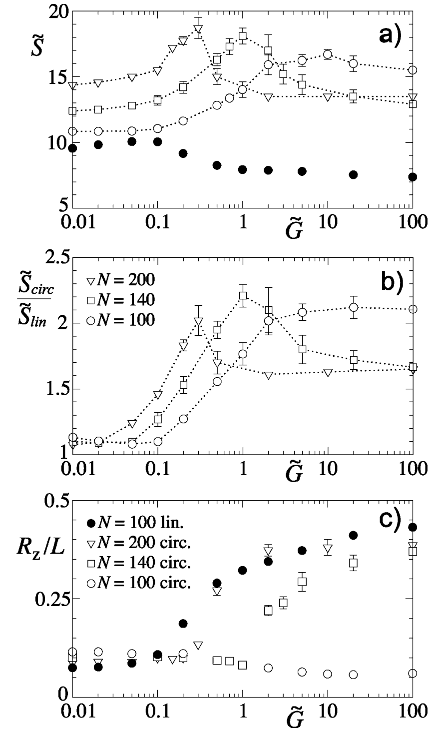

Figure 10. Sedimentation coefficient (a) and (b) and relative extension (c) of *circular* (open symbols) and *linear* chains (filled symbols), all for SA-FJC with full hydrodynamic interactions (HI). For better comparison with the circular chains, the values for R_z/L of the filled symbols are divided by a factor of 2.

logarithmic corrections proportional to the number of monomers in the tail divided by the tail length. For the two longer chains the limiting ratio of two is not yet reached. This fact could be exploited for an efficient separation of linear from circular chains because a factor of 2 can easily be resolved in ultracentrifugation experiments, whereas the molecular weight dependence is only logarithmic according to eq 19. The ratio of the sedimentation constant of a circular to a linear chain with the same monomer number increases nonmonotonically from a value close to one at small fields to a value slightly below two in the limit of long chains and high fields (see Figure 10b). This limit is not yet reached in the simulation.

Contrary to linear chains (see Figure 1a), the curves of $\tilde{S}(\tilde{G})$ of different N cross each other in Figure 10a. An intermediate regime as in eq 34 does not exist for the chain lengths investigated. However, it is not clear whether this situation persists for very long circular chains; it is conceivable that due to the strong steric effects the curves for $N \le 200$ cross each other while much longer chains do not. Such a behavior is also seen for $\tilde{S}(\tilde{G})$ of the linear $N = 40$ chain, which crosses the $N = 100$ curves at $\tilde{G} \approx 3$. Experiments are needed to clarify this point.

5. The Preaveraging Approximation and Phantom Chain Results

To gain better understanding of the nonequilibrium nature of the phenomenon and the importance of hydrodynamics, we also perform simulations in the preaveraging approximation (PAA). Since the velocity then is independent of the chain conformation, the following quantity is used as an estimate for the sedimentation coefficient:[7]

$$\bar{S} = \frac{3a}{4N}\sum_{i\neq j}\left\langle \frac{1}{r_{ij}} + \frac{{z_{ij}}^2}{{r_{ij}}^3}\right\rangle \tag{44}$$

The brackets represent the configurational average at a given field G. This expression can be derived as follows: From eqs 1 and 12 we obtain by using the Oseen tensor eq 6 for $i \neq j$ and the Stokes mobility for the self-part $i = j$ the following expression

$$\tilde{S}^{(\mathrm{Os})} = \frac{\langle \tilde{v}_z\rangle}{N\tilde{G}} = \frac{1}{N^2\tilde{G}}\sum_{i=0}^{N}\langle \hat{e}_z\cdot\dot{\mathbf{r}}_i\rangle$$

$$= \frac{1}{N^2\tilde{G}}\sum_{i=0}^{N} \hat{e}_z\cdot\Bigg\langle \mu_0\mathbf{I}\cdot[-\nabla_{\mathbf{r}_i}U + G\hat{e}_z] + \sum_{j\neq i}\frac{3a\mu_0}{4r_{ij}}\left[\mathbf{I} + \frac{\mathbf{r}_{ij}\otimes\mathbf{r}_{ij}}{{r_{ij}}^2}\right]\cdot[-\nabla_{\mathbf{r}_j}U + G\hat{e}_z]\Bigg\rangle \tag{45}$$

where we used that $\langle \xi_i\rangle = 0$. For $N \gg 1$ we can neglect the diagonal with respect to the off-diagonal part of the mobility (this amounts to the so-called "nondraining approximation"). If we additionally assume that the internal forces $-\nabla_{\mathbf{r}_j}U$ cancel out,[7] eq 45 goes over to eq 44. For long chains the average inverse distance between two monomers becomes small so that eq 44 is also a good approximation for the Rotne−Prager HI case, eq 3. Note that for an isotropic random coil $\bar{S}$ reduces to the rescaled inverse hydrodynamic radius defined by $a\sum\langle {r_{ij}}^{-1}\rangle/N$.[26]

In Figure 11, we study the influence of the PAA and the SA property on the sedimentation anomaly and compare $\bar{S}$ for three cases, (a) Gaussian PC (circles), eq 10 and $\epsilon_{\mathrm{LJ}} = 0$, (b) SA Gaussian (squares), eq 10 and $\epsilon_{\mathrm{LJ}} = 1$, (c) SA FJC (triangles), eq 9 and $\epsilon_{\mathrm{LJ}} = 1$, each for both, full hydrodynamics (HI, open symbols), eqs 3 and 4, and PAA (filled symbols), eq 5. We use a chain length $N = 40$ and divide the results by the zero-field limit $\bar{S}(G{=}0)$. Zimm's PAA calculation (solid line) for an ideal Gaussian chain at small fields[7]

$$\frac{\bar{S}(G)}{\bar{S}(0)} \approx 1 - 0.02887\,[0.0391N^{3/2}\tilde{G}]^2 + 0.00205[0.0391N^{3/2}\tilde{G}]^4 + \mathcal{O}(N^{3/2}\tilde{G})^6 \tag{46}$$

describes quantitatively both the HI and PAA simulations of an ideal Gaussian chain (circles). At small fields, i.e., close to equilibrium, the difference between PAA and HI is hardly visible for phantom chains, justifying Zimm's PAA for weak perturbations. The slight difference between the simulations (filled circles) and eq 46 is most likely due to the finite chain length and the neglect of higher-order terms. We thus reproduce with our $N = 40$ results Zimm's original formula[7] and not the corrected one[6] where $\tilde{G}$ is replaced by $\tilde{G}/2$. No increase of $\bar{S}$ is seen for these PC, meaning that hydrodynamic compaction is absent for phantom chains. This is understandable because the compaction is caused by entanglement effects between recirculating polymer sections. Self-avoidance effects drastically change the simulation results; in addition, the difference between PAA and HI becomes more pronounced for SA chains. The approximation $\bar{S} \approx \tilde{S}$ is tested by including in Figure 11 a few points of $\tilde{S}(\tilde{G})/\tilde{S}(0)$, as defined in eq 12, simulated with HI: For Gaussian PC the results for the relative decrease of $\tilde{S}$ (stars) and $\bar{S}$ (open circles) nearly agree and are both well described by eq 46; for SA-FJC the quantity $\bar{S}(\tilde{G})/\bar{S}(0)$ (open squares)

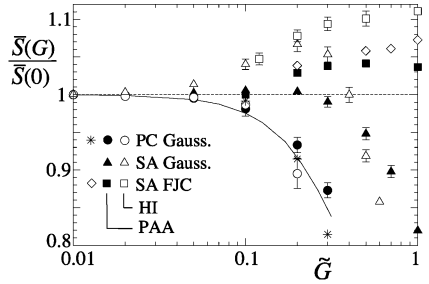

Figure 11. Relative approximate sedimentation coefficient $\bar{S}(G)/\bar{S}(0)$ as defined in eq 44 for a linear $N = 40$ chain modeled as a self-avoiding freely jointed chain (SA-FJC, squares), SA Gaussian (triangles), and Gaussian phantom chain (PC) (circles). Open symbols include full hydrodynamics (HI); filled ones use the preaveraging approximation (PAA). The solid line is Zimm's PAA calculation eq 46 for an Gaussian PC.[7] In addition, we show some data points of $\tilde{S}(G)/\tilde{S}(0)$ for a SA-FJC (diamonds) and an Gaussian PC (stars), both with HI.

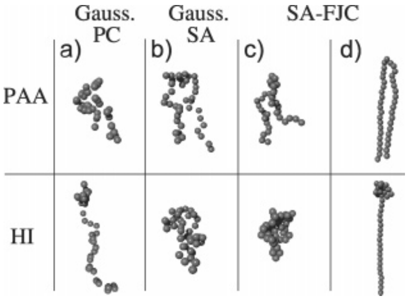

Figure 12. Conformations of a Gaussian phantom chain (PC) (a), self-avoiding (SA) Gaussian chains (b), and SA freely jointed chain (FJC) (c) at $\tilde{G} = 0.3$, as well as SA-FJC at $\tilde{G} = 10$ (d). The upper row uses the preaveraging approximation (PAA) and the lower row full Rotne–Prager hydrodynamic interactions (HI).

can only reproduce the right trend of $\tilde{S}(\tilde{G})/\tilde{S}(0)$ (diamonds). It is thus justified to measure the sedimentation constant by $\bar{S}$ for Gaussian PC at low field strengths, as long as one is only interested in the relative decrease with respect to its zero-field value.[7,11]

Despite the partial success to predict the sedimentation constant at small fields for phantom chains, the PAA gives qualitatively wrong predictions: As already noted, the preaveraging approach yields no sedimentation anomaly for circular chains[7,9] since all points along the chain are equivalent. Figure 12a–c shows snapshots for the six situations, three types of chains each for PAA and HI, at a small field strength $\tilde{G} = 0.3$: If a PAA is used, the coils are deformed in a way that both ends lag behind (upper row). HI unfold or compact the chains (lower row). At high fields, a linear SA-FJC in the PAA shows a configuration where both tails are trailing and the symmetry-breaking between the two tails is not obtained, while with full HI the known tadpole form appears (see Figure 12d). To conclude, self-avoidance affects the sedimentation anomaly in an essential way even for smaller fields; at high fields, full HI are indispensable.

6. Birefringence

Sedimentation velocity experiments can only indirectly test our predicted configurational changes. Optical measurements may provide additional and often complementary information. In a birefringence experiment the difference of the refractive index in the sedimentation direction and a direction perpendicular to it, Δn, is measured which is proportional to the following *birefringence parameter*[27]

$$\chi = \frac{1}{2(N-1)}\sum_{i=1}^{N-1}[3\cos\phi_i - 1] \tag{47}$$

where ϕ_i is the angle the ith bond vector forms with the sedimentation field. χ is thus a measure for the average orientation of the bond vectors: $\chi = 1$ means that all bond vectors are parallel to the sedimentation force and $\chi = -0.5$ that they are all perpendicular to it.

In Figure 13, we show χ as a function of $\tilde{G}$ for different chain lengths. Surprisingly, not only stretching but also compaction (as observed with the data for $N = 20$) leads to a positive birefringence signal indicative of chain orientation. Long chains ($N = 200$) show a Kerr-type behavior at small fields, $\chi \propto \tilde{G}^2$. This is expected on the basis of our results for the chain stretching in the weak-stretching regime, which is also quadratic in the sedimentation field. In general, χ displays a complex dependence on $\tilde{G}$, reflecting the different regimes discussed in the previous sections. For the $N = 40$ chain, for instance, χ is proportional to $\tilde{G}$ and exhibits a non-Kerr-type behavior, $\chi \propto \tilde{G}$, in the range $0.1 \le \tilde{G} \le 1$. The mechanism for this scaling behavior is most likely related to recirculation in the compactified chain.

7. Semiflexibility Effects

A quantitative prediction of the DNA sedimentation anomaly[6] is at present not feasible, since the nonuniversal dependence on the ratio of chain diameter and persistence length is not included. A more direct comparison of our predictions might be possible with synthetic chains, where this complication is absent. For DNA strands with radius $a \approx 1$ nm, persistence length $l_P \approx 50$ nm, and a contour length L in the micrometer to millimeter range, the scale separation $a \ll l_P \ll L$ renders a realistic simulation impractical. To provide some insight into the possible effects one expects for semiflexible polymers, we add a bending energy term U_b to the elastic potential $U_{el}^{(FJC)}$ in eq 9:

$$U_b = l_P\sum_{i=2}^{N-1}\frac{k_BT}{2a}[1 - \cos\theta_i] \tag{48}$$

Here θ_i is the angle between consecutive bonds $\mathbf{r}_{i-1i}$ and $\mathbf{r}_{ii+1}$. In Figure 14, we show result for a $N = 100$ linear SA FJC with full hydrodynamic interactions (HI) as an example and plot $\tilde{S}/N^{1-\nu}$ and χ as a function of the rescaled persistence length l_P/L at an elevated field strength $\tilde{G} = 1$. At this field strength one obtains a tadpole configuration in the limit of vanishing persistence length $l_P = 0$. The curves for the sedimentation coefficient $\tilde{S}$ and the orientational order parameter χ are both nonmonotonic, and their form will depend in addition to l_P/L and $\tilde{G}$ also on the aspect ratio L/a; this deserves, of course, further investigation in the future. A nonzero but small persistence length, $a \ll l_P \ll L$, leads to a looser head and thus a shorter tail, resulting in a slight increase of sedimentation speed $\tilde{S}$. At $l_P \sim L$ we observe a crossover from a tadpole configuration to a bent rod, as shown by the snapshots in Figure 14b. Accordingly, the sedimentation shows a slight dip. For further increasing persistence length, the orientational order parameter χ finally becomes negative, indicative of a perpendicular orientation with respect to the sedimentation direction. This effect was introduced and rationalized in detail in ref 28 and is caused by the bending of the rod into a horseshoe shape. A perpendicular rod exhibits a higher frictional coefficient than a parallel rod, which explains the decrease of $\tilde{S}$ and χ for $\tilde{G} \ge 30$. As can be appreciated from Figure 14a, the sedimentation behavior of

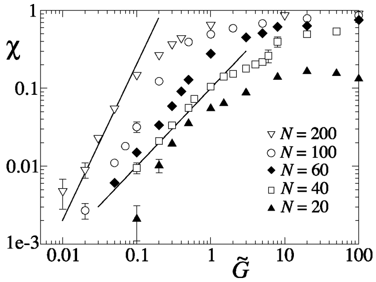

Figure 13. Birefringence parameter χ defined in eq 47 as a function of the sedimentation field $\tilde{G}$ for linear SA FJC with HI. The lines are guides to the eye with slopes one and two.

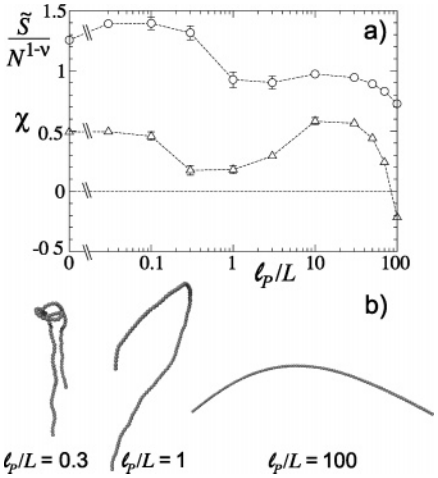

Figure 14. (a) Rescaled sedimentation coefficient $\tilde{S}/N^{1-\nu}$ with ν = 3/5 (circles) and birefringence parameter χ (triangles) as a function of the relative persistence length l_P/L for a $N = 100$ linear SA FJC with HI at $\tilde{G} = 1$. The left-most data points are obtained by setting $l_P = 0$ and correspond to the previously shown flexible chain results. (b) Snapshots of typical chain conformations at rescaled persistence lengths $l_P/L = 0.3$, 1, and 100. A crossover from parallel orientation for flexible chains to perpendicular orientation for stiff chains is observed.

a semiflexible polymer at elevated sedimentation fields gives rise to a number of competing effects and tendencies, and no unified, simple picture emerges. More work along these lines is necessary.

8. Discussion

To check the experimental relevance of our results, we consider the particular system of ref 6, namely a 115 × 10^6 Da DNA strand in a centrifuge with radius $R_{UC} = 0.052$ m spinning at a frequency of $60\omega/2\pi = 50\,000$ rpm. For a direct comparison we need to specify the size of the effective monomer of the DNA chain. A naive choice would be one base pair. In this case, however, the monomer would be a very oblate nonspherical object, which is impractical for numerical simulations. If we demand that the effective monomer be spherical having the same diameter as DNA, i.e., a radius of $a = 1$ nm, one monomer would correspond to approximately six base pairs if we assume a rise per base pair of 0.34 nm. For an average mass of 615 Da per base pair this gives a mass per monomer of $m_0 = (2/0.34) \times 615$ Da ≈ 3618 Da. We use a buoyancy correction factor of $1 - \rho_w/\rho_{DNA} = 0.436$, where ρ_w and ρ_{DNA} are the densities of water and DNA, and obtain a rescaled field of

$$\tilde{G} = m_0\left[1 - \frac{\rho_w}{\rho_{DNA}}\right]R_{UC}\omega^2\frac{a}{k_BT} \sim 10^{-6} \qquad (49)$$

Using an effective monomer number of $N = 30\,000$, the theoretically predicted critical unfolding field $\tilde{G}^\star$ is, according to eq 29, $\tilde{G}^\star \sim 7 \times 10^{-7}$ and thus of the same order. This means that based on our simulation results and scaling relations the onset of chain unfolding for long DNA chains should be observable in typical ultracentrifuge experiments (in agreement with the experimental fact).

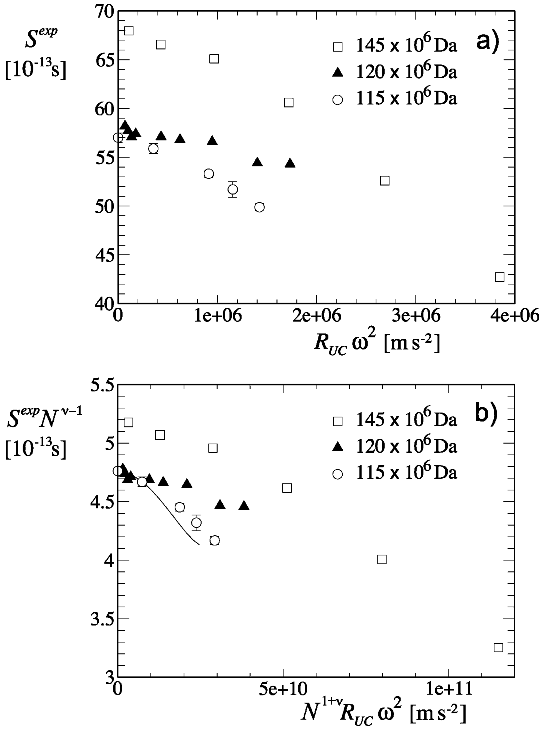

Figure 15. (a) Experimental sedimentation coefficients of linear DNA strands with 145 × 10^6,[9] 120 × 10^6,[3] and 115 × 10^6 Da[6] vs the radial acceleration $R_{UC}\omega^2$, assuming a buoyancy correction factor of $1 - \rho_w/\rho_{DNA} = 0.436$ and centrifuge radii R_{UC} of 9.8, 6.3, and 5.2 cm, respectively. (b) Rescaled experimental data where effective monomer numbers N of 625, 518, and 496 (top to bottom) are assumed and a Flory exponent of $\nu = 3/5$. The line is Zimm's formula eq 46 with a monomer number fitted to the third data set, $N = 496$.

How does the finite persistence length of DNA change this estimate? The persistence length of DNA is under physiological conditions $l_P \approx 50$ nm and thus much smaller than the contour length, which in our example is $L \approx 60$ μm, but it is considerably larger than the diameter of the effective monomer of $2a = 2$ nm. To account for persistence length effects, one could in a simplistic approach use an effective monomer diameter $2a_2$ equal to the Kuhn statistical segment length $2l_P$,[29] i.e. $a_2 = l_P \approx 50a$, with an effective monomer number $N_2 = Na/l_P$ reduced by a factor of 50. Such a reparametrization scheme was suggested previously,[7,11] but especially for short polymers is not totally accurate due to specific semiflexibility effects explored in section 7. Following eqs 29 and 49, the reparametrization would increase both the critical rescaled field $\tilde{G}^\star$ and the experimentally realized rescaled field $\tilde{G}$ by a factor of $a_2^2/a^2 = 2500$ since both the effective monomer mass $m_0^{(2)} = M/N_2$ and radius $a_2 = L/(2N_2)$ are inversely proportional to N_2 where M is the polymer mass. The ratio $\tilde{G}/\tilde{G}^\star$ is thus invariant with respect to this reparametrization and our above estimate of the threshold for DNA unfolding is unchanged.

Figure 15 shows a compilation of data of three ultracentrifuge measurements on DNA: for 145 × 10^6 Da strands,[9] for 120 × 10^6 Da,[3] and for 115 × 10^6 Da.[6] Neglecting the uncertainty of the precise solvent density in the sucrose measurements, we assume for all three cases a buoyancy correction factor of $1 - \rho_w/\rho_{DNA} = 0.436$. For the radii of the centrifuges R_{UC} in these experiments we take the values 9.8, 6.3, and 5.2 cm, where it should be noted that these numbers are estimates and inferred indirectly by us using the ultracentrifuge specifications given in the original publications. One can see a decrease of S^{exp} qualitatively similar to the small field result depicted in Figure 6a (the strong stretching regime is not yet reached) but on the other hand notices quite large differences between the data which cannot be explained solely by the different DNA lengths. This is brought out more clearly in Figure 15b where the data are rescaled using effective monomer numbers which are chosen proportional to the molecular weight. We here follow Zimm's data analysis and assign to the third data set (115×10^6 Da) a monomer number of $N = 496$. Using the average mass of 615 Da per DNA base pair, this choice corresponds to an effective monomer comprising 377 base pairs with a contour length of 118 nm. Figure 15b shows the rescaled data together with Zimm's theory eq 46 for a corresponding monomer number of $N = 496$ (solid line). The perfect agreement between Zimm's theory and one data set for small gravitational fields reflects the fact that the effective monomer number has been freely adjusted. Note that the framework of eq 46 would imply a scaling $S(0) \propto N^{1/2}$, in contradiction to the experimentally observed $S(0) \propto N^{0.38}$ for long DNA strands.[30] Likewise, the correct slope of eq 46 possibly is coincidental as self-avoidance effects are neglected which were shown to be important even at small sedimentation fields. Most importantly, it is seen that the experimental zero-field sedimentation data do not collapse. The reason for this is unclear, and it poses a serious problem for the quantitative comparison between theory and experiments. Clearly, more experiments are desirable. For reasons mentioned before, a direct application of eq 26 or eq 46 is not possible since semiflexibility effects are neglected in the theory. In fact, for the naive choice of a monomer radius of 1 nm both equations would give numbers outside the range of Figure 15a and thus have to be discarded. Using the effective monomer number as a free fitting parameter allows to describe experimental data accurately, but this fitting parameter unfortunately lacks a clear physical meaning.

Unfolding of polymers in elongational and shear flow has experimentally been intensely investigated,[31,32] whereas unfolding in homogeneous flow has not been considered probably due to the smallness of the effects compared to the other types of flow at typical shear rates. We have argued that it can be still very important for long polymers at high centrifugation speeds. Hydrodynamics are essential since all effects vanish in the free-draining approximation. The compaction predicted for short chains (see Figure 1b for $N = 10$ and $N = 20$) might be similar in nature to the conformational changes under sedimentation of certain proteins which lead to an increase of the sedimentation coefficient.[33] Increase of S at high rotor speed is also observed for semidilute solutions of long DNA, which was, however, attributed to aggregation.[34] The oscillatory behavior in Figure 9c has been seen in simulations at finite Reynolds number.[35] A systematic investigation of the influence of excluded volume, HI, and finite extensibility on the viscosity of a very dilute polymer solution has been undertaken in ref 36 which might be fruitful to compare with the presented sedimentation results.

The unfolding transition might also be relevant in the context of electrophoresis if strong enough electric fields lead to fast motion. Here a different unfolding mechanism due to electric polarization effects is operative.[37] It should be noted that tadpole-like structures also appear in gel electrophoresis at high fields.[38,39] Although their physical origin is most likely quite different, a detailed comparison of both stretching mechanisms might be worthwhile.

Acknowledgment. We are thankful to Helmut Coelfen and Holger Straus from the Max-Planck-Insitut for Colloids and Interfaces for discussions. Financial support by the Bavarian Elite Fund Complex Interfaces and the Deutsche Forschungsgemeinschaft (SPP1164) is acknowledged.

Note Added after ASAP Publication. This article was published ASAP on February 16, 2008. Several minor text changes, including two equation references, have been made. The correct version was published on February 19, 2008.

References and Notes

(1) Harding, S. E.; Rowe, A. J.; Horton, J. C. *Analytical Ultracentrifugation in Biochemistry and Polymer Science*; Royal Society of Chemistry: Cambridge, UK, 1993.
(2) Laue, T. M.; Stafford, W. F. *Annu. Rev. Biophys. Biomol. Struct.* **1999**, *28*, 75.
(3) Rubenstein, I.; Leighton, S. B. *Biophys. Chem.* **1974**, *1*, 292.
(4) Chia, D.; Schumaker, V. N. *Biochem. Biophys. Res. Commun.* **1974**, *56*, 241.
(5) Hutchinson, F.; Krasin, F. *Biophys. Chem.* **1977**, *6*, 23.
(6) Clark, R. W.; Lange, C. S. *Biopolymers* **1980**, *19*, 945.
(7) Zimm, B. H. *Biophys. Chem.* **1974**, *1*, 279.
(8) Ertas, D.; Kardar, M. *Phys. Rev. E* **1993**, *48*, 1228.
(9) Ralston, E. J.; Schumaker, V. N. *Biophys. Chem.* **1979**, *9*, 375.
(10) Schlagberger, X.; Netz, R. R. *Phys. Rev. Lett.* **2007**, *98*, 128301.
(11) Zimm, B. H.; Schumaker, V. N.; Zimm, C. B. *Biophys. Chem.* **1976**, *5*, 265.
(12) Ermak, D. L.; McCammon, J. A. *J. Chem. Phys.* **1978**, *69*, 1352.
(13) Rotne, J.; Prager, S. *J. Chem. Phys.* **1969**, *50*, 4831.
(14) Doi, M.; Edwards, S. F. *The Theory of Polymer Dynamics*; Clarendon Press: Oxford, 1986.
(15) Cooke, I. R.; Williams, D. R. M. *Europhys. Lett.* **2003**, *64*, 267.
(16) Tirado, M. M.; López Martínez, C.; García de la Tore, J. *J. Chem. Phys.* **1984**, *81*, 2047.
(17) A movie showing the recirculation and unfolding can be downloaded from the authors Web page http://einrichtungen.physik.tu-muenchen.de/T37/xaver.html.
(18) Happel, J.; Brenner, H. *Low Reynolds Number Hydrodynamics*; Kluwer: The Hague, 1983.
(19) de Gennes, P.-G. *Scaling Concepts in Polymer Physics*; Cornell University Press: Ithaca, NY, 1979.
(20) Schlagberger, X.; Bayer, J.; Rädler, J. O.; Netz, R. R. *Europhys. Lett.* **2006**, *76*, 346.
(21) García Bernal, J. M.; Tirado, M. M.; Freire, J. J.; García de la Torre, J. *Macromolecules* **1991**, *24*, 593.
(22) García de la Torre, J.; Carrasco, B. *Prog. Colloid Polym. Sci.* **1999**, *113*, 81.
(23) Pincus, P. *Macromolecules* **1976**, *9*, 386.
(24) Pettijohn, D.; Hecht, R. M.; Stimpson, D.; van Scoyk, S. *J. Mol. Biol.* **1978**, *119*, 353.
(25) Odijk, T. *Colloids Surf. A* **2002**, *210*, 191.
(26) Kirkwood, J. G. *J. Polym. Sci.* **1954**, *12*, 1.
(27) Elvingson, C. *Biophys. Chem.* **1992**, *43*, 9.
(28) Schlagberger, X.; Netz, R. R. *Europhys. Lett.* **2005**, *70*, 129.
(29) Netz, R. R.; Andelman, D. *Phys. Rep.* **2003**, *380*, 1.
(30) Freifelder, D. *J. Mol. Biol.* **1970**, *54*, 567.
(31) Shaqfeh, E. S. G. *J. Non-Newtonian Fluid Mech.* **2005**, *130*, 1.
(32) Larson, R. G. *J. Rheol.* **2005**, *49*, 1.
(33) Borges, J. C.; Fischer, H.; Craievich, A. F.; Ramos, C. H. I. *J. Biol. Chem.* **2005**, *280*, 13671.
(34) Rosenbloom, J.; Schumaker, V. *Biochemistry* **1967**, *6*, 276.
(35) Lehtola, V.; Punkkinen, O.; Ala-Nissila, T. *Phys. Rev. E* **2007**, *76*, 051802.
(36) Pamies, R.; Lopez Martinez, M. C.; Hernandez Cifre, J. G.; Garcia de la Torre, J. *Macromolecules* **2005**, *38*, 1371.
(37) Netz, R. R. *Phys. Rev. Lett.* **2003**, *90*, 128104.
(38) Kaji, N.; Ueda, M.; Baba, Y. *Biophys. J.* **2002**, *82*, 335.
(39) Calladine, C. R.; Drew, H. R.; Luisi, B. F.; Travers, A. A. *Understanding DNA*, 3rd ed.; Elsevier: Amsterdam, 2004.

MA070947M